

Improving Photostability of Cesium-Doped Formamidinium Lead Triiodide Perovskite

Anthony Donakowski, D. Westley Miller, Nicholas C. Anderson, Anthony Ruth, Erin M. Sanehira, Joseph J. Berry, Michael D. Irwin, Angus Rockett, and K. Xerxes Steirer*



Cite This: *ACS Energy Lett.* 2021, 6, 574–580



Read Online

ACCESS |



Metrics & More

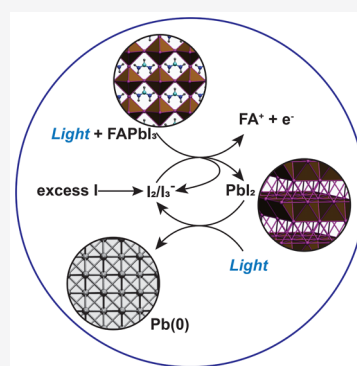


Article Recommendations



Supporting Information

ABSTRACT: Using time-resolved *in situ* X-ray photoelectron spectroscopy, we identify and suppress rapid degradation mechanisms for cesium-stabilized formamidinium lead iodide perovskite materials used in state-of-the-art photovoltaics. Accelerated degradation under high light intensity and heating reveals a photocatalytic reaction pathway responsible for rapid decomposition in iodide-rich compositions and a slower pathway for more stoichiometric samples. Using Avrami–Erofe’ev kinetic analysis, we find that the fast process is consistent with a 2D crystallization and growth mechanism fueled by excess halide salt at grain boundaries and surfaces. Moreover, the rate of decomposition varies dramatically with the wavelength of light used to illuminate the thin films. Our results reveal the photodegradation mechanisms of PbI_2 and excess iodide and provide a path to increasing perovskite stability under photoexcitation.



Metal halide perovskites (MHPs) are at the center of heightened research efforts due to their remarkable semiconducting properties achieved through facile processing routes.¹ Rapid material improvements have led to high-quality optoelectronic properties, such as sharp Urbach edges across a wide range of band gaps and deposition methods,^{2,3} enabling new solar cell technologies with unprecedented increases in power conversion efficiency.⁴ In fact, these new MHP solar cells are approaching and may soon surpass the record efficiency of single-crystal silicon solar cells.⁴ However, intrinsic and extrinsic stability issues still plague MHP materials.^{5,6}

Approaches to improving the MHP stability include alloying all or some sites in the ABX_3 structure as well as engineering 2D molecular overlayers, evaluating additives, and designing contact passivation.^{7–11} For example, alloying the A-site formamidinium (FA) with Cs to form Cs:FAPbI₃ stabilizes the α -phase perovskite via Goldschmidt tolerance tuning.^{12,13} Christians et al. demonstrated a highly alloyed MHP-based solar cell with stability up to 1000 h unencapsulated in ambient.¹⁴ Bai et al. reported an extrapolated 5200 h for an encapsulated planar MHP solar cell that used an ionic liquid additive.¹⁰ Additional stabilization opportunities include leveraging MHP self-healing defects.¹⁵ Yet, fundamental degradation mechanisms must be elucidated to realize the decades of operational stability desired for perovskite photovoltaic utility-scale deployment.¹⁶

Several recent publications suggest that both the initial performance and light-induced degradation pathways are very

sensitive to the balance of AX and BX_2 in the MHP. Tumen-Ulzii et al. reported on *ex situ* studies of unreacted PbI_2 in a $\text{Cs}_{0.05}(\text{FA}_{1-x}\text{MA}_x)_{0.95}\text{Pb}(\text{I}_{1-y}\text{Br}_y)_3$ system, where excess PbI_2 increased device failure.¹⁷ However, Merdasa et al. reported beneficial recombination kinetics when excess PbI_2 is present and well mixed.¹⁸ PbI_2 reversibly photodegrades,¹⁹ which may result in metallic lead defects that can pin the Fermi level near the conduction band minimum, reducing photovoltage.²⁰ The effects of excess organic A-site cation and precursors on MHP stability have also been investigated.²¹ Wei et al. reported that light degrades some organic MHP precursors, particularly in the presence of I_2 .²² Juarez-Perez et al. found both reversible and irreversible photodecomposition pathways for methylammonium lead iodide,²³ whereas Boyd and co-workers found the incorporation of excess AX to improve hole contact performance.²⁴

Halide defects and impurities further complicate the issue of MHP stability and are known to redistribute under illumination.²⁵ It has been observed that halide vacancies V_X are highly mobile and can produce giant contact polarization at the electron contact, improving charge collection, reducing

Received: November 5, 2020

Accepted: January 5, 2021

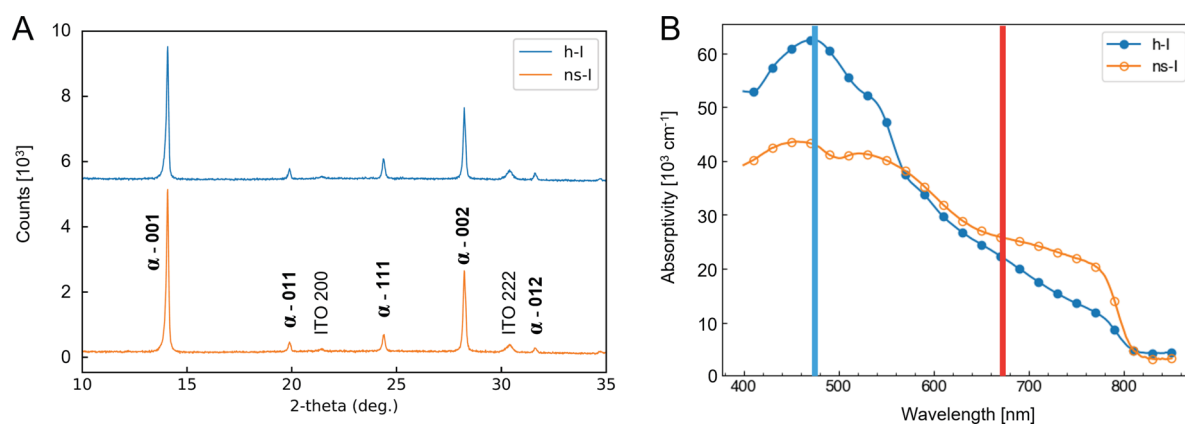


Figure 1. (A) XRD patterns for h-I and ns-I samples, vertically offset for clarity. (B) UV–vis absorptivity for the same samples, corrected for refractive index and surface roughness. Note that h-I and ns-I samples have I:Pb ratios of 3.8 and 2.8, respectively.

hysteresis, and increasing device efficiency.²⁶ However, Aristidou et al. have shown that an abundance of V_I provides a pathway for oxygen ingress into the MHP.²⁷ Calculations by Liu and co-workers showed that excess halide in MHPs changes the degradation landscape by eliminating halide vacancies and produces a chemical environment favorable for halide interstitials (X_i).²⁸ Tan et al. reported that I_i aggravates the instability in FAPbI₃ perovskites.²⁹ In solutions containing dichloromethane, illumination of mixed-halide MHPs selectively expels halide ions, suggesting facile release of I species.^{30,31} Other reports suggest I_3^- may also play an important role in MHP degradation.^{29,31} On the other hand, Yang et al. showed that excess iodide, added as I_3^- , improved device performance by eliminating deep level defects.³² Meanwhile, employing excess PbI₂ to boost device performance has come under scrutiny due to PbI₂ photolysis.³³ These widely ranging observations point to the importance of MHP compositions for both performance and longevity. What may be observed for one MHP film type may not be observed for another. New studies directly monitoring film stoichiometry are needed to elucidate the underlying mechanisms of MHP decomposition and failure of photovoltaic devices in working environments.

Here, we show how MHP stoichiometry alters the dominant photochemical decomposition mechanism using *in situ* X-ray photoelectron spectroscopy (XPS), a surface-sensitive analysis technique well suited for the identification and separation of MHP degradation mechanisms. Cs-stabilized formamidinium lead triiodide (Cs:FAPbI₃) is a state-of-the-art MHP for high-performance solar cells.⁸ We compare different stoichiometries of this MHP with red-light (671 nm) and blue-light (473 nm) exposure at high power densities, revealing the production of metallic lead via a multi-step process photocatalyzed in the presence of excess I. Films with near-stoichiometric compositions are remarkably stable in comparison and degrade via a different mechanism. We discuss our findings in terms of defect chemistries, chemical reactions, and impacts on device stability.

We compared Cs:FAPbI₃ films having different compositions which resulted in very different photostabilities. Sample names are chosen to represent their relative halide content. We define sample names explicitly as h-I = high I:Pb ratio and ns-I = near-stoichiometric I:Pb ratio.

X-ray diffraction (XRD) results for the h-I and ns-I samples are shown in Figure 1A. Both h-I and ns-I samples are α -phase

perovskites³⁴ and produce nearly identical diffraction patterns. Minor differences are discussed in detail in the Supporting Information (SI) (Figure S1). A small signal from the underlying ITO substrate is also observed.

Visible light absorptivity plots for h-I and ns-I films are shown in Figure 1B, which were corrected for refraction and surface roughness effects (please see SI, Figure S2, for raw data). When compared to the sample ns-I, sample h-I exhibits weaker absorptivity at the red edge and increased absorptivity between 400 and 580 nm. The absorptance regions are assessed in detail below, and additional analysis is provided in the SI (Figure S2). Blue and red lines represent laser wavelengths used in this study.

Time-resolved XPS data provides quantitative elemental information correlated with chemical environments. Cs:FAPbI₃ thin films were illuminated with 671 nm (red) or 473 nm (blue) light in the XPS (see SI, Figure S3). Laser illumination (1000 mW/cm²) is spread over the analyzed sample area (800 μ m diameter circle) and confined to the measured area by the lens aperture. Repeated control XPS experiments in the dark showed only 3–5% loss of I at room temperature and 10–15% loss of I at 69 °C, with zero Pb(0) intensity observed after a 10 h exposure to X-rays in a vacuum. In contrast, methylammonium lead triiodide (MAPI) loses two-thirds of its I in less than 10 h at room temperature in XPS experiments.³⁵ Therefore, *in situ* XPS data reported here is within a time frame where X-ray damage does not produce a significant effect on Cs:FAPbI₃.

The I:Pb ratios were determined using I 3d_{5/2} and Pb 4f core levels and a calibration factor based on several neat PbI₂ films (SI, Figure S4 and Table S1). Different pieces of the same samples were tested under different illumination conditions. Pb 4f data and fit results for Cs:FAPbI₃ samples heated to 69 °C and exposed to blue light (1000 mW/cm²) are shown in Figure 2. Figure 2A provides a normalized intensity map with the Pb 4f_{7/2} feature on the right and the Pb 4f_{5/2} feature on the left, with a doublet separation of 4.87 eV. Spectral feature binding energy (BE) positions and assignments are plotted as dashed lines on the Pb 4f_{5/2} signal. Analysis routines are described in detail in the SI (Figures S4 and S5). Light exposure induces a small but stable negative shift in all core levels which varied slightly for the different samples.

For the data from the h-I sample shown in Figure 2A, the Pb 4f_{7/2} signal associated with Cs:FAPbI₃ is located at 137.4 eV, whereas the signal centered at 137.9 eV is associated with PbI₂.

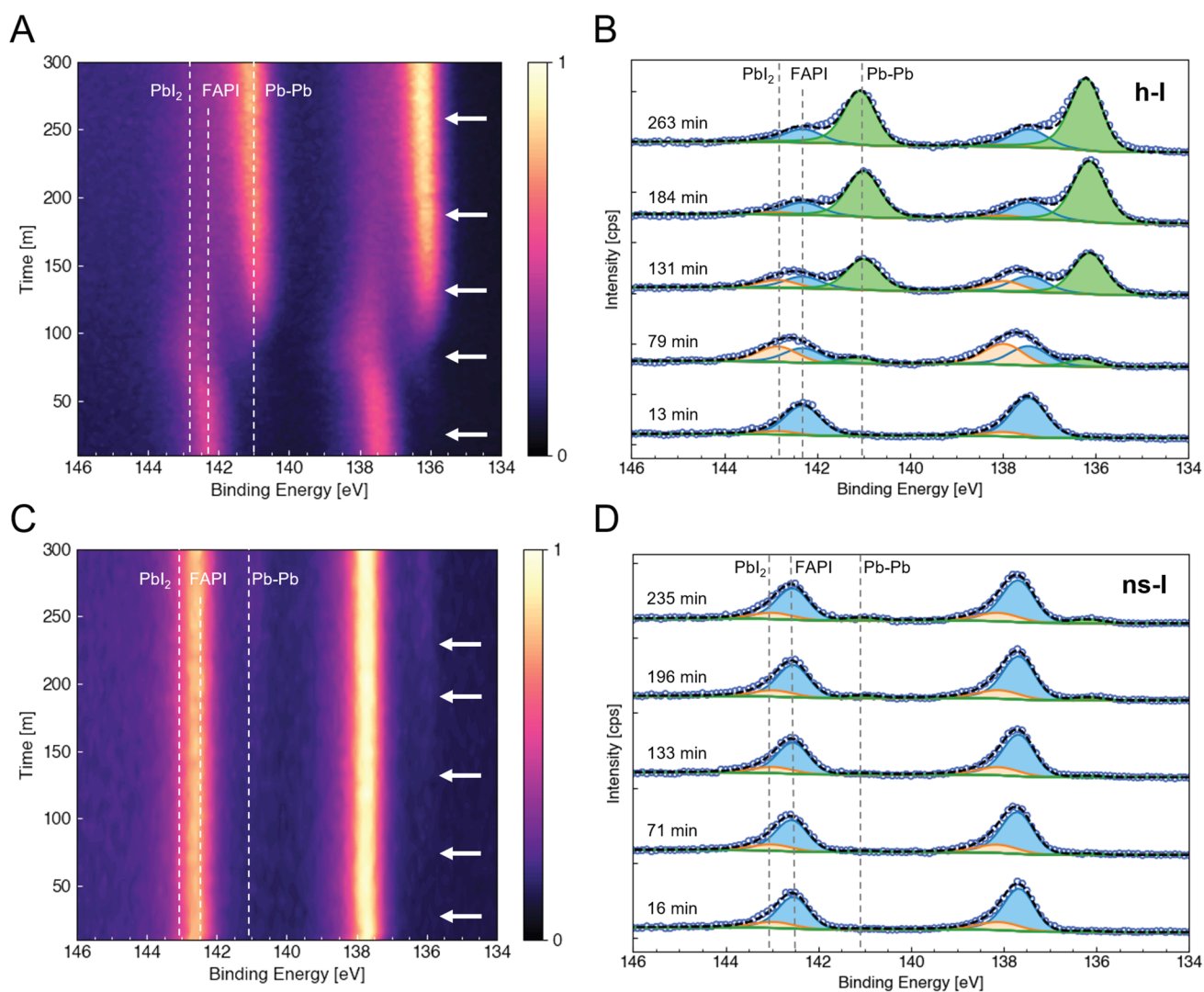


Figure 2. Time-resolved *in situ* XPS spectra and fits for blue-laser-exposed perovskite samples with I/Pb = 3.8 (A, B) and 2.8 (C, D). (A, C) Intensity map Pb 4f core-level spectra with time increasing from bottom to top. Dotted white lines indicate centroid positions. (B, D) Fit results for spectra marked with arrows in panels A and C.

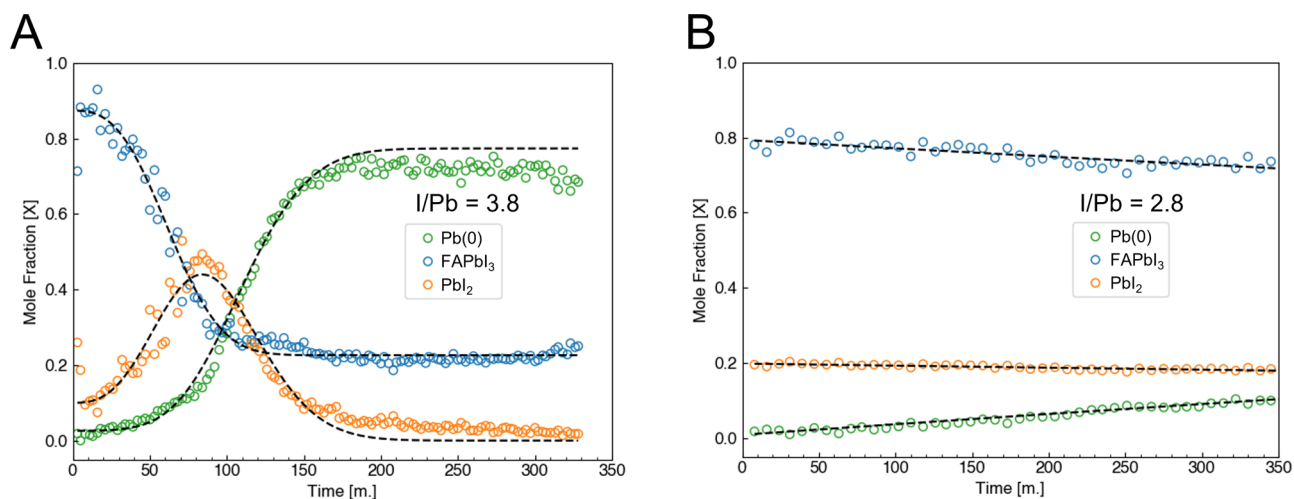


Figure 3. Time-resolved *in situ* XPS Pb 4f areal fit results from h-I (A) and ns-I (B) perovskite samples. Molar fraction (χ) of Pb is normalized by the total Pb 4f signal.

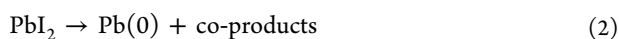
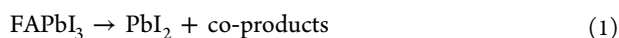
Blue-light exposure over time shows the emergence of a third peak at 136.1 eV, associated with Pb(0).³⁶ These illuminated

BE values are lower than average reference values³⁷ for MHPs deposited on TiO₂ by 0.5–0.8 eV, due primarily to the NiO p-

type back contact as described by Schulz et al.³⁸ White arrows in Figure 2A correspond to spectra in Figure 2B. The intensity of the PbI₂ feature significantly increases after 50 min of exposure to blue light, followed by a rapid increase in the Pb(0) signal (second spectra from bottom, Figure 2B). At longer times, the Pb(0) signal dominates the spectra. Additional XPS core-level analysis indicates that the I/Pb ratio falls to below 1.5 ± 0.15, concurrent with decreasing N 1s signal. Figure 2C,D shows the time-resolved Pb 4f spectra for the ns-I perovskite under identical test conditions. A 0.18 eV BE shift of the ns-I sample relative to the h-I sample is observed. The ns-I sample exhibits higher photostability, as the Pb(0) signal emerges relatively slowly.

The Pb 4f peak area fit results of the time-resolved *in situ* XPS data from the h-I sample under blue-light illumination are shown in Figure 3A. These are normalized to the raw Pb 4f area and plotted as molar fraction of Pb [χ]. At early times the Cs:FAPbI₃ spectral intensity (blue circles) is decreasing, the PbI₂ intensity (orange circles) is increasing, and the emergence of the Pb(0) signal (green circles) is observed. FAPI loss is commensurate with the increased PbI₂ signal intensity. Between 70 and 90 min, the PbI₂ intensity maximum coincides with rapid loss of Cs:FAPbI₃ and increasingly rapid growth of Pb(0). Figure 3B shows the peak area fit results for the ns-I sample. A slower loss of Cs:FAPbI₃ signal is observed with a slow rise of Pb(0). The PbI₂ signal is steady, with a small negative slope. A 10% molar fraction of Pb(0) is found to occur 10 times slower in the ns-I sample when compared to the h-I sample. In contrast, the growth rate for Pb(0) under red-light illumination is minuscule (SI, Figure S6).

The XPS data implies the following two-step reaction for photodecomposition of perovskite under blue-light conditions:



The Avrami–Erofe'ev (A-E) equation describes the time-dependent concentration of solid phases during conversion at fixed temperature and was applied to reactions 1 and 2. The general form of the A-E equation for the concentration of a species in the perovskite is

$$[A] = [B]_0 - \Delta[B](1 - e^{-(kt)^n}) \quad (3)$$

where [A] is the time-dependent concentration of Pb(0) or PbI₂, [B] is the total change in concentration during the reaction, [B]₀ is the initial concentration, *k* is the rate constant, *t* is time, and *n* is the Avrami parameter. Changes to concentration follow nucleation and growth where product phases grow in *n* - 1 dimensions. Hence, the resulting value for *n* has morphological consequences ranging from zero- (*n* = 1) to three-dimensional (*n* = 4) phase conversion fronts. Fits to the lead data curves in Figure 3 (dashed lines) yielded Avrami parameters of *n* = 2.75 for the h-I sample and *n* = 1 for the ns-I sample. Fitting of the h-I blue exposure data with a coupled two-step A-E model (SI, Table S2) revealed reaction rate constants *k*₁ = 0.014 and *k*₂ = 0.0091 χ /min for eqs 1 and 2, respectively. For the ns-I sample, the reaction rates were *k*₁ = 0.00029 and *k*₂ = 0.0014 χ /min, respectively.

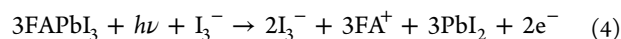
The Avrami parameter for the h-I sample (*n* = 2.75) suggests 2D layer growth of PbI₂, whereas the Avrami parameter for the ns-I sample (*n* = 1) suggests a homogeneous conversion to PbI₂ by nucleation only. In both cases, the same *n* fits the time-dependent Cs:FAPbI₃ loss, PbI₂ increase and decrease, and

Pb(0) increase. Therefore, the reaction kinetics indicate that the degradation morphology is dependent on the PbI₂ nucleation and growth mechanism. In the h-I film, PbI₂ growth is 1.5 times faster than PbI₂-to-Pb(0) conversion, which allows for expansion of the phase front and layered growth. Conversely, for the ns-I film, the PbI₂ is converted to Pb(0) 5 times faster than it is created, and therefore it nucleates and is converted before growth can occur.

Excess halide will induce compositional effects including a range of defects and, in extreme cases such as this, non-perovskite phases. The I:Pb ratio of 3.8 and excess N indicate a FAI-rich matrix for the h-I sample. The most likely halide impurity to exist in this case is iodide dissolved in non-crystalline phases balanced with excess FA complexes. Analysis of the I 3d_{5/2} reveals increased photoelectron intensity at higher BE not belonging to Cs:FAPbI₃ (SI, Figure S4). Similar analysis of the N 1s core level shows a broad increase in intensity relative to the ns-I sample. The signatures strongly support the existence of I₃⁻, in agreement with an earlier XPS study examining MHP products formed *in situ* under a gold overlayer³⁹ and a recent report by Mundt et al.⁴⁰

The majority of wavelength-dependent absorbance below 600 nm will be broadly affected by this superstoichiometric composition of FA_{*x*}PbI_{*y*}, where *x* > 1 and *y* > 3. Pure polycrystalline FAPbI₃ is relatively featureless from 400 to 800 nm,⁴¹ whereas MHPs grown with excess FAI in a vacuum and in solution have been reported to produce materials with second-phase inclusions.^{42,43} Analysis of the absorbance data in Figure 1B shows that the observed increase below 600 nm is coincident with decreased absorptivity at the band edge when excess FAI is present. Therefore, excess FAI consumes FAPbI₃, forming second-phase inclusions (e.g., I₂, FA₂PbI₄). Although unlikely to be present, any unreacted FAI in the h-I sample would also photodegrade and produce reactive products that further decompose the perovskite.²²

The I:Pb ratio alone, 3.8:1, implies a substantial mole fraction of iodide that interstitials could not contain without compromising the crystalline solid. Iodide is too large, and the majority of excess halide will be present in amorphous phases at grain boundaries and surfaces. Under light, iodine is more likely present as I₃⁻, not I₂, because the standard potential of the iodide/triiodide redox couple is only 0.35 V versus the normal hydrogen electrode (NHE).⁴⁴ The photo-assisted triiodide redox mechanism is as follows:

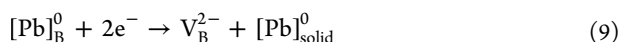
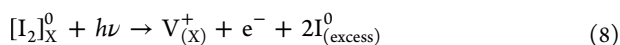


where excess iodine produces a chemical environment favorable to the production of triiodide, in addition to the triiodide already present in the film. Decomposition of FA is implicit in reaction 4, where the FA cations may decompose. The perovskite is decomposed to lead following reactions 4 and 5. The photocatalyst triiodide is further produced following reaction 6.

FAI-rich conditions will favor the formation of crystallographic point defects (FA_{*v*}, I_{*v*}, and H-centers) in the h-I perovskite.²⁸ A high concentration of FAI increases the likelihood of iodine-rich defects such as I₂⁻ and I₃⁻ interstitials. Moreover, the triiodide defect has a broad absorbance centered at 500 nm and will contribute to the increased

absorbance of blue light. While inclusions of PbI_2 could potentially enhance absorbance at 471 nm,¹⁹ this is inconsistent with the I:Pb ratio observed in the h-I sample, and no sharp step is observed at the PbI_2 band gap in Figure 1B.

A photoactivated mechanism for perovskite decomposition with excess iodine that assumes some excess iodide is contained within the crystalline bulk can be expressed using Kröger–Vink notation as follows:



where excess I and hole capture lead to H-center-type defects following $h^+ + \text{X}_X^0 + \text{X}_i^- \leftrightarrow [\text{X}_2]_X^0$, implicit in reaction 7. Whalley et al. speculate that the perovskite could form redox-active polyanion inclusions, facilitating additional electron or hole trapping,⁴⁵ thus accelerating photocatalytic decomposition of the perovskite material (reactions 7 and 8). The reduction of Pb^{2+} in reaction 9 is consistent with the observed formation of $\text{Pb}(0)$ (Figure 2). Under blue-light illumination, $\text{Pb}(0)$ forms much faster in neat PbI_2 films (SI, Figure S7) than in either of the Cs:FAPi films, suggesting reaction 9 is not the rate-limiting step of perovskite photodecomposition. Furthermore, the formation of I_2 during photodecomposition of PbI_2 also contributes to the blue-absorbing excess iodine defects, resulting in accelerated Cs:FAPi decomposition in the h-I sample.

Halide depletion is expected in the ns-I sample, forming I vacancies (V_I). Analysis of XRD results in Figure 1A indicates a very small peak shift of (00 l) indices for the h-I sample relative to the ns-I sample. This observation suggests that variations of I content may only subtly affect crystallographic planes without compromising the perovskite crystal structure. Given the above discussion on excess I, a contraction of the (00 l) spacing and the I:Pb ratio of 2.8 indicate the presence of V_I defects in the ns-I sample. Mobile halide vacancies are known to strongly impact the photocurrent and defect concentrations at surfaces and interfaces.⁴⁶ V_I are related to PbI_2 inclusions, device improvements, and several degradation pathways, including aggregation of Schottky defect clusters, phase transformation, and diffusion of oxygen into the MHP.⁴⁷ The UV–vis absorptivity of ns-I films shown in Figure 1B exhibits stronger band edge absorptivity yet lower absorbance, attributable to fewer defects and impurities, as discussed above. Moreover, the 0.18 eV Fermi level shift away from the valence level compared with the h-I sample likely results from a voltage drop at the NiO contact, as described by Boyd et al.²⁴ The charge-balanced defect for highly mobile V_I is V_{FA} . These Schottky defect pairs can combine to form PbI_2 nucleation centers as follows:



Slow accumulation of these vacancies produces PbI_2 that, when formed, rapidly converts to $\text{Pb}(0)$ under blue-light illumination.

Neither PbI_2 photolysis nor perovskite photodegradation caused by iodine-rich defects or triiodide impurities would be excited by red light, which is consistent with significantly lower rates of decomposition observed under red-light illumination (SI, Figures S6 and S7) and a report by Quitsch et al. showing

MHP photodegradation occurring only for photons having energy above the metal halide band gap.⁴⁸

The generation of layered products in the h-I case is much faster than the homogeneous degradation in the ns-I case. The h-I samples produce volatile species that readily react at interfaces and surfaces. In a vacuum under illumination, the generation and release of I species from the perovskite surface have been observed.^{49,50} On the other hand, the ns-I case is limited by the mobility of Schottky defect pairs. Calculations for near-stoichiometric MHP materials with a non-zero population of V_I indicate interstitial formation energies with positive slopes and lower formation energies under illumination. Excess I, however, leads to I_i formation energies with negative slopes.²⁸ Illumination increases the formation energy of interstitials and causes excess I to form photoactive $\text{I}_2(\text{g})$, which can combine with an I^- and contribute to the rapid MHP degradation.

Observing both $\text{Pb}(0)$ and Cs:FAPi at the end of the reaction implies that the thickness is less than the XPS probe depth (ca. 10 nm), in agreement with the 2D layered model for the h-I sample. Upon photoexcitation, the perovskite decomposes, forming PbI_2 primarily at grain boundaries and surfaces.⁵¹ Photolysis is related to the local concentration of PbI_2 , which leads to $\text{Pb}(0)$ nucleation and growth and terminates with a 20% mole fraction of Cs:FAPi remaining in the h-I sample. The high rate of ion diffusion in both the Cs:FAPi and PbI_2 means few nuclei are needed to drive degradation and precipitation of products at surfaces and interfaces at early times. At later times, the closed-lattice $\text{Pb}(0)$ may prevent halide vacancy migration and volatile product outgassing, similar to the effect of Bi deposition,⁵² and thereby limit total decomposition to the surface in the h-I case.

Limiting the formation of I_3^- is clearly important due to its photoactivity, which catalyzes the degradation of MHP materials. Additionally, controlling the stoichiometry of MHPs to restrict reactions that form BX_2 impurities may also be necessary for stabilizing MHP photovoltaics. In practice, however, the full solar cell stack and the surrounding environment must be considered. Encapsulating MHP materials in a solar device may involve the presence of volatile species (i.e., I_2) and allow for healing of the $\text{Pb}(0)$ defects in the dark by reversal of PbI_2 photolysis. On the other hand, I_2 may also undergo photolysis and irreversibly react with the perovskite or contact layers within the photovoltaic device.²¹ In the extreme case where triiodide impurities are abundant, photocatalytic degradation may be difficult to avoid and likely impossible to reverse in the dark. At the MHP interfaces, contact layers will also affect defect concentrations. Under illumination, the quasi Fermi level will reside near the dominant charge transport level, and in one promising study, the hole transport layer stabilized V_I by nearly 1 eV compared to I_i .²⁸

Through kinetic analysis using *in situ* XPS experiments on state-of-the-art Cs:FAPi perovskite films, we identified key mechanisms for perovskite photodecomposition fueled by defects and impurities which are activated by blue-light exposure. These deleterious species can be controlled through careful manipulation of perovskite stoichiometry, yielding MHPs with significantly lower photodegradation after several hours of X-ray exposure under high illumination at elevated temperatures.

■ ASSOCIATED CONTENT

SI Supporting Information

The Supporting Information is available free of charge at <https://pubs.acs.org/doi/10.1021/acseenergylett.0c02339>.

Detailed experimental procedures and descriptions of analysis techniques; sample preparation, XRD, UV-absorbance, XPS methods, and figures; description of the Avrami–Erofe'ev analysis; and red- vs blue-light Pb(0) comparisons for Cs:FAPbI₃ and PbI₂ (PDF)

■ AUTHOR INFORMATION

Corresponding Author

K. Xerxes Steirer – Physics Department, Colorado School of Mines, Golden, Colorado 80401, United States; orcid.org/0000-0001-6137-2105; Email: ksteirer@mines.edu

Authors

Anthony Donakowski – Physics Department, Colorado School of Mines, Golden, Colorado 80401, United States
D. Westley Miller – Hunt Perovskite Technologies LLC, Dallas, Texas 75201, United States
Nicholas C. Anderson – Hunt Perovskite Technologies LLC, Dallas, Texas 75201, United States
Anthony Ruth – Hunt Perovskite Technologies LLC, Dallas, Texas 75201, United States
Erin M. Sanehira – Hunt Perovskite Technologies LLC, Dallas, Texas 75201, United States
Joseph J. Berry – National Renewable Energy Laboratory, Golden, Colorado 80401, United States
Michael D. Irwin – Hunt Perovskite Technologies LLC, Dallas, Texas 75201, United States
Angus Rockett – Department of Metallurgical and Materials Engineering, Colorado School of Mines, Golden, Colorado 80401, United States; orcid.org/0000-0001-9759-8421

Complete contact information is available at <https://pubs.acs.org/doi/10.1021/acseenergylett.0c02339>

Notes

The authors declare the following competing financial interest(s): Authors D.W.M., A.R., E.M.S., and M.D.I. are employed by Hunt Perovskite Technologies, a metal halide perovskites focused research and development company. N.C.A. was employed by Hunt Perovskite Technologies from 2017 through 2020.

■ ACKNOWLEDGMENTS

This work is funded by the U.S. Department of Energy Solar Energy Technologies Office, under Award Number DE-EE0008540. The authors would like to thank Kai Zhu and Fei Zhang from NREL for their contributions.

■ REFERENCES

- (1) Snaith, H. J. Present status and future prospects of perovskite photovoltaics. *Nat. Mater.* **2018**, *17*, 372–376.
- (2) Miller, D. W.; Eperon, G. E.; Roe, E. T.; Warren, C. W.; Snaith, H. J.; Loneragan, M. C. Defect states in perovskite solar cells associated with hysteresis and performance. *Appl. Phys. Lett.* **2016**, *109*, 153902.
- (3) Sutter-Fella, C. M.; et al. Band Tailing and Deep Defect States in CH₃NH₃Pb(I_{1-x}Br_x)₃ Perovskites As Revealed by Sub-Bandgap Photocurrent. *ACS Energy Lett.* **2017**, *2*, 709–715.
- (4) Kopidakis, N. Best Research Cell Efficiencies. <https://www.nrel.gov/pv/assets/pdfs/best-research-cell-efficiencies.20200925.pdf> (accessed 11/2020).
- (5) Shahivandi, H.; Vaezzadeh, M.; Saeidi, M. Theory of light-induced degradation in perovskite solar cells. *Sol. Energy Mater. Sol. Cells* **2020**, *208*, 110383.
- (6) Zhou, Y.; Zhao, Y. Chemical stability and instability of inorganic halide perovskites. *Energy Environ. Sci.* **2019**, *12*, 1495–1511.
- (7) Tosado, G. A.; Lin, Y.-Y.; Zheng, E.; Yu, Q. Impact of cesium on the phase and device stability of triple cation Pb-Sn double halide perovskite films and solar cells. *J. Mater. Chem. A* **2018**, *6*, 17426–17436.
- (8) Gao, X.-X.; et al. Stable and High-Efficiency Methylammonium-Free Perovskite Solar Cells. *Adv. Mater.* **2020**, *32*, 1905502.
- (9) Liu, Y.; et al. Stabilization of highly efficient and stable phase-pure FAPbI₃ Perovskite Solar Cells by Molecularly Tailored 2D-Overlayers. *Angew. Chem., Int. Ed.* **2020**, *59* (36), 15688–15694.
- (10) Bai, S.; et al. Planar perovskite solar cells with long-term stability using ionic liquid additives. *Nature* **2019**, *571*, 245–250.
- (11) Tan, H.; et al. Efficient and stable solution-processed planar perovskite solar cells via contact passivation. *Science* **2017**, *355*, 722–726.
- (12) Li, Z.; et al. Stabilizing Perovskite Structures by Tuning Tolerance Factor: Formation of Formamidinium and Cesium Lead Iodide Solid-State Alloys. *Chem. Mater.* **2016**, *28*, 284–292.
- (13) Lee, J.-W.; et al. Formamidinium and Cesium Hybridization for Photo- and Moisture-Stable Perovskite Solar Cell. *Adv. Energy Mater.* **2015**, *5*, 1501310.
- (14) Christians, J. A.; et al. Tailored interfaces of unencapsulated perovskite solar cells for > 1,000 h operational stability. *Nat. Energy* **2018**, *3*, 68–74.
- (15) Nie, W.; et al. Light-activated photocurrent degradation and self-healing in perovskite solar cells. *Nat. Commun.* **2016**, *7*, 1–9.
- (16) Dunfield, S. P.; et al. From Defects to Degradation: A Mechanistic Understanding of Degradation in Perovskite Solar Cell Devices and Modules. *Adv. Energy Mater.* **2020**, *10*, 1904054.
- (17) Tumen-Ulzii, G.; et al. Detrimental Effect of Unreacted PbI₂ on the Long-Term Stability of Perovskite Solar Cells. *Adv. Mater.* **2020**, *32* (16), 1905035.
- (18) Merdasa, A.; et al. Impact of Excess Lead Iodide on the Recombination Kinetics in Metal Halide Perovskites. *ACS Energy Lett.* **2019**, *4*, 1370–1378.
- (19) Dawood, R. I.; Forty, A. J.; Tubbs, M. R.; Frank, F. C. The photodecomposition of lead iodide. *Proc. Royal Soc. London. Ser. A. Math. Phys. Sci.* **1965**, *284*, 272–288.
- (20) Zu, F.; et al. Surface State Density Determines the Energy Level Alignment at Hybrid Perovskite/Electron Acceptors Interfaces. *ACS Appl. Mater. Interfaces* **2017**, *9*, 41546–41552.
- (21) Wang, S.; Jiang, Y.; Juarez-Perez, E. J.; Ono, L. K.; Qi, Y. Accelerated degradation of methylammonium lead iodide perovskites induced by exposure to iodine vapour. *Nat. Energy* **2017**, *2*, 1–8.
- (22) Wei, H.; Chen, S.; Zhao, J.; Yu, Z.; Huang, J. Is Formamidinium Always More Stable than Methylammonium? *Chem. Mater.* **2020**, *32*, 2501–2507.
- (23) Juarez-Perez, J.; et al. Photodecomposition and thermal decomposition in methylammonium halide lead perovskites and inferred design principles to increase photovoltaic device stability. *J. Mater. Chem. A* **2018**, *6*, 9604–9612.
- (24) Boyd, C. C.; et al. Overcoming Redox Reactions at Perovskite-Nickel Oxide Interfaces to Boost Voltages in Perovskite Solar Cells. *Joule* **2020**, *4*, 1759–1775.
- (25) deQuilettes, D. W.; et al. Photo-induced halide redistribution in organic-inorganic perovskite films. *Nat. Commun.* **2016**, *7*, 11683.
- (26) Kim, H.-S.; et al. Control of I - V Hysteresis in CH₃NH₃PbI₃ Perovskite Solar Cell. *J. Phys. Chem. Lett.* **2015**, *6*, 4633–4639.
- (27) Aristidou, N.; et al. Fast oxygen diffusion and iodide defects mediate oxygen-induced degradation of perovskite solar cells. *Nat. Commun.* **2017**, *8*, 15218.
- (28) Liu, N.; Yam, C. First-principles study of intrinsic defects in formamidinium lead triiodide perovskite solar cell absorbers. *Phys. Chem. Chem. Phys.* **2018**, *20*, 6800–6804.

- (29) Tan, S.; et al. Shallow Iodine Defects Accelerate the Degradation of a-Phase Formamidinium Perovskite. *Joule* **2020**, *4*, 2426–2442.
- (30) Mathew, P. S.; Samu, G. F.; Janáky, C.; Kamat, P. V. Iodine (I) Expulsion at Photoirradiated Mixed Halide Perovskite Interface. Should I Stay or Should I Go? *ACS Energy Lett.* **2020**, *5*, 1872–1880.
- (31) Samu, G. F.; et al. Electrochemical Hole Injection Selectively Expels Iodide from Mixed Halide Perovskite Films. *J. Am. Chem. Soc.* **2019**, *141*, 10812–10820.
- (32) Yang, W. S.; et al. Iodide management in formamidinium-lead-halide-based perovskite layers for efficient solar cells. *Science* **2017**, *356*, 1376–1379.
- (33) Roose, B.; Dey, K.; Chiang, Y.-H.; Friend, R. H.; Stranks, S. D. Critical Assessment of the Use of Excess Lead Iodide in Lead Halide Perovskite Solar Cells. *J. Phys. Chem. Lett.* **2020**, *11*, 6505–6512.
- (34) Weller, M. T.; Weber, O. J.; Frost, J. M.; Walsh, A. Cubic Perovskite Structure of Black Formamidinium Lead Iodide, a-[HC(NH₂)₂]₂PbI₃, at 298 K. *J. Phys. Chem. Lett.* **2015**, *6*, 3209–3212.
- (35) Steirer, K. X.; Schulz, P.; Teeter, G.; Stevanovic, V.; Yang, M.; Zhu, K.; Berry, J. J. Defect Tolerance in Methylammonium Lead Triiodide Perovskite. *ACS Energy Lett.* **2016**, *1*, 360–366.
- (36) Xiao, W.; et al. Exploring Red, Green, and Blue Light-Activated Degradation of Perovskite Films and Solar Cells for Near Space Applications. *Sol. RRL* **2020**, *4*, 1900394.
- (37) Béchu, S.; Ralaifarisoa, M.; Etcheberry, A.; Schulz, P. Photoemission Spectroscopy Characterization of Halide Perovskites. *Adv. Energy Mater.* **2020**, *10*, 1904007.
- (38) Schulz, P.; et al. Electronic Level Alignment in Inverted Organometal Perovskite Solar Cells. *Adv. Mater. Interfaces* **2015**, *2*, 1400532.
- (39) Kerner, R. A.; et al. Reactions at noble metal contacts with methylammonium lead triiodide perovskites: Role of underpotential deposition and electrochemistry. *APL Mater.* **2019**, *7*, 041103.
- (40) Mundt, L. E.; et al. Surface-Activated Corrosion in Tin-Lead Halide Perovskite Solar Cells. *ACS Energy Lett.* **2020**, *5*, 3344–3351.
- (41) Nazarenko, O.; Yakunin, S.; Morad, V.; Cherniukh, I.; Kovalenko, M. V. Single crystals of caesium formamidinium lead halide perovskites: solution growth and gamma dosimetry. *NPG Asia Mater.* **2017**, *9*, e373–e373.
- (42) Jia, Y.-H.; et al. Role of Excess FAI in Formation of High-Efficiency FAPbI₃-Based Light-Emitting Diodes. *Adv. Funct. Mater.* **2020**, *30*, 1906875.
- (43) Reinoso, M.; Otálora, C. A.; Gordillo, G. Improvement Properties of Hybrid Halide Perovskite Thin Films Prepared by Sequential Evaporation for Planar Solar Cells. *Materials* **2019**, *12*, 1394.
- (44) Boschloo, G.; Hagfeldt, A. Characteristics of the Iodide/Triiodide Redox Mediator in Dye-Sensitized Solar Cells. *Acc. Chem. Res.* **2009**, *42*, 1819–1826.
- (45) Whalley, L. D.; Crespo-Otero, R.; Walsh, A. H-Center and V-Center Defects in Hybrid Halide Perovskites. *ACS Energy Lett.* **2017**, *2*, 2713–2714.
- (46) Bertoluzzi, L.; et al. Mobile Ion Concentration Measurement and Open-Access Band Diagram Simulation Platform for Halide Perovskite Solar Cells. *Joule* **2020**, *4*, 109–127.
- (47) Boyd, C. C.; Cheacharoen, R.; Leijtens, T.; McGehee, M. D. Understanding Degradation Mechanisms and Improving Stability of Perovskite Photovoltaics. *Chem. Rev.* **2019**, *119*, 3418–3451.
- (48) Quitsch, W.-A.; et al. The Role of Excitation Energy in Photobrightening and Photodegradation of Halide Perovskite Thin Films. *J. Phys. Chem. Lett.* **2018**, *9*, 2062–2069.
- (49) Zu, F.; et al. Position-locking of volatile reaction products by atmosphere and capping layers slows down photodecomposition of methylammonium lead triiodide perovskite. *RSC Adv.* **2020**, *10*, 17534–17542.
- (50) Hofstetter, Y. J.; et al. Vacuum-Induced Degradation of 2D Perovskites. *Front. Chem.* **2020**, *8*, 8.
- (51) Marchezi, P. E.; et al. Degradation mechanisms in mixed-cation and mixed-halide Cs_xFA_{1-x}Pb(Br_yI_{1-y})₃ perovskite films under ambient conditions. *J. Mater. Chem. A* **2020**, *8*, 9302–9312.
- (52) Wu, S.; et al. A chemically inert bismuth interlayer enhances long-term stability of inverted perovskite solar cells. *Nat. Commun.* **2019**, *10*, 1161.

Improving Photostability of Caesium Doped Formamidinium Lead Triiodide Perovskite - Supporting Information

Anthony Donakowski¹, D. Westley Miller², Nicholas C. Anderson², Anthony Ruth², Erin M. Sanehira², Joseph J. Berry³, Michael D. Irwin², Angus Rockett⁴, and K. Xerxes Steirer^{1,*}

¹Colorado School of Mines, Physics Department, Golden CO 80401, USA

²Hunt Perovskite Technologies LLC., Dallas TX 75201, USA

³National Renewable Energy Lab, Golden CO 80401, USA

⁴Colorado School of Mines, Department of Metallurgical and Materials Engineering, Golden CO 80401, USA

*ksteirer@mines.edu

1 Sample Preparation

Thin film perovskite samples were prepared on indium tin oxide (ITO) coated glass substrates (Delta Technologies, Ltd.). The ITO-coated glass is cleaned via sonication in detergent, deionized water, isopropanol, and acetone, sequentially. Directly prior to thin film deposition, the ITO surface is cleaned via oxygen plasma for 5 min. Nickel oxide is deposited from a molecular ink and annealed using methods similar to previous reports.¹ A mixed-cation Cs:FAPbI₃ perovskite thin film is deposited using a two-step method and annealed to remove residual solvent.²⁻⁴ Films are deposited via blade-coating on 50 mm substrates in humidity-controlled glove boxes.

2 XRD

Coupled X-ray diffraction scans (gonio) were sequentially measured on both h-I and ns-I samples in ambient using an Empyrean X-ray Diffractometer with a Cu X-ray source. The XRD was equipped with an incident mirror (BBHD) to remove K_β X-rays and a hybrid pixel detector (Galipix 3D) for fast data acquisition. Divergence was 1/16°. Soller slits were used to minimize the measured peak asymmetries. Several short repeated scans were taken in order to identify possible X-ray damage, which was not observed. Figure S1 shows the measured diffraction patterns for the h-I and ns-I samples as well as their normalized difference. Both h-I and ns-I samples showed only α -phase perovskite and small signals from the underlying ITO substrate. The difference plot in Figure S1C indicates a slight peak shift of the (001) and (002) peaks, suggesting that the h-I sample d-spacing is slightly larger than the ns-I sample for these crystal planes. Additionally, having been normalized to the (001) peak, the h-I sample shows slightly increased peak intensity and no observable shift for the remaining perovskite diffraction peaks (011), (111) and (012). This observation suggests that the h-I sample is slightly less textured in the substrate normal direction relative to the ns-I sample. These data indicate the h-I and ns-I samples are nearly identical w.r.t. diffraction. However, the h-I sample exhibits a slight increase in d-spacing for (001) indices and a reduction of the weak texture relative to the ns-I sample. Hence, the amount of FAI present in Cs:FAPbI₃ does have a slight but measurable impact on the bulk structure.

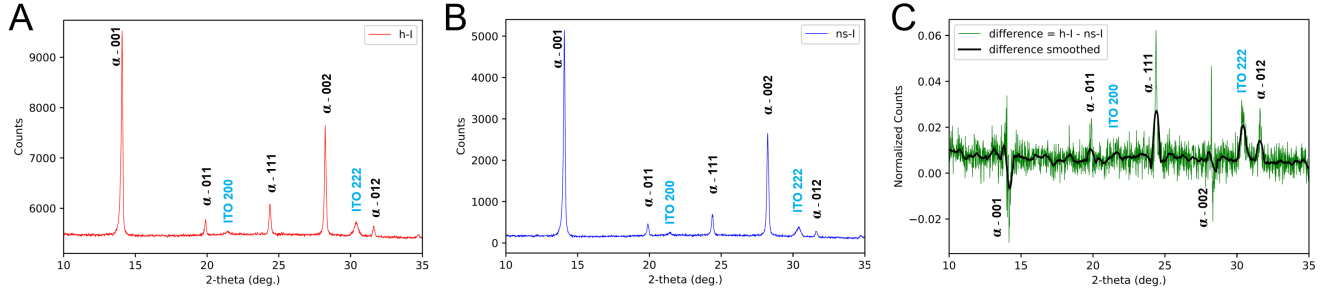


Figure S1. XRD of h-I and ns-I Cs:FAPI thin films. A) h-I sample. B) ns-I sample. C) Difference calculated from normalized A - B showing subtle shift in peak positions for (001), (002) and intensities for (011), (111), (012) indices.

3 Absorbance Analysis

UV-Vis absorbance spectra of thin films were obtained using a 150 mm integrating sphere module on a Perkin Elmer Lambda 900 UV-Vis spectrometer. The samples were set at 15 degrees angle of incidence on a clip in the middle of the integrating sphere so that specular reflectance was captured by the sphere and would not be mistaken for absorbance. The monochromator slits were set for 2 nm resolution. Data were acquired in 5 nm steps from 850 to 400 nm with 1 second integration per data point. A 100 % Transmission correction was applied using the Perkin-Elmer software to account for the differences between the sample and reference beam optical paths.

The formula applied to the analysis of raw absorbance data shown in Figure S2 is intended to achieve an estimate of the increased path length for light transmitted into the perovskite film as a function of wavelength. It is based on the following:

Light passing through a film of thickness t at an angle x relative to normal and neglecting Fresnel cavity interferences will go through a total distance d of material on its first pass to the back surface according to

$$d = t / \cos(x) \quad (1)$$

Thicknesses were 332 nm for the h-I sample and 302 nm for the ns-I sample. According to Snell's law, light passing from a material with index of refraction n_1 into a material with n_2 will be bent, shifting its angle of incidence x_1 to an angle of transmission x_2 according to:

$$x_2 = \arcsin([n_2/n_1] \times \sin(x_1)) \quad (2)$$

Substituting x_2 for x in 1 and assuming $n_1 = 1$ (vacuum, and close enough for air) yields the effective path length correction as a function of wavelength.

Average surface angles resulting from surface roughness were found to be 18° for the h-I sample and 7° for the ns-I sample as expected due to the different FAI concentrations. The data in this case have had a roughness assigned to the near stoichiometric film that brings it into agreement with literature values at its band edge. The h-I sample was then adjusted so that the subgap absorption for both films matches. It is very weak in both cases and reveals a lower absorption coefficient for the h-I film at the gap and a higher coefficient in the blue where I-rich impurities absorb strongly.

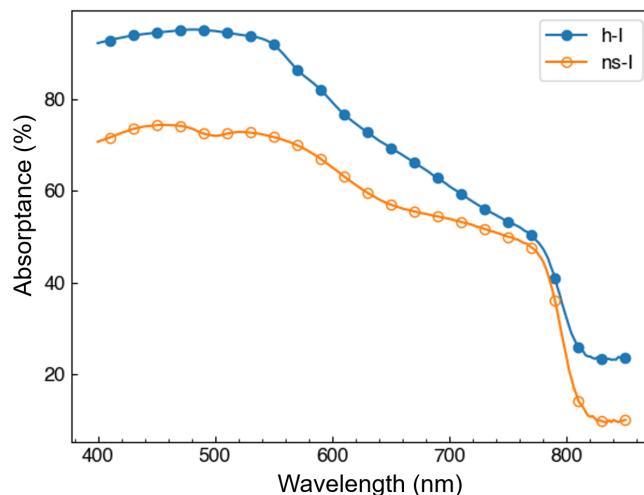


Figure S2. Raw absorbance measured for h-I and ns-I Cs:FAPbI₃ thin films before path length corrections.

4 XPS Methods

XPS was performed on a HiPP-3 system equipped with a line of sight viewport to the sample directly from the analyzer. Monochromatic Al K α X-rays are focused on the sample surface and liberate core level electrons from atoms within the sample surface region. Photoelectron kinetic energy is measured and subtracted from the exciting X-ray energy (1496.7 eV) following the well known photoelectric effect. The result is photoelectron intensity versus electron binding energy (BE). BE calibration was done on clean Au foil using the established Au 4f_{7/2} = 83.98 eV. Illumination of the MHPs resulted in a small BE shift, which stabilized after a single scan. The laser was defocused to an 800 μ m diameter circle at the position of the sample. An 800 μ m diameter aperture was positioned 800 μ m from the sample surface and the tip of which is visible in Figures S3A and S3B. Laser intensity was calibrated using a Hamamatsu silicon photodiode with known responsivity. Laser power was 1000 mW/cm² for red and blue laser exposures, equal to 10 suns power density. Analysis of *in situ* XPS data was performed using in house code written in Python. Surface temperature calibration was done on Cs:FAPbI₃ thin films by visual inspection of melting 99.9% pure In metal on the surface while slowly cycling the temperature up and down across the solid-liquid transition.

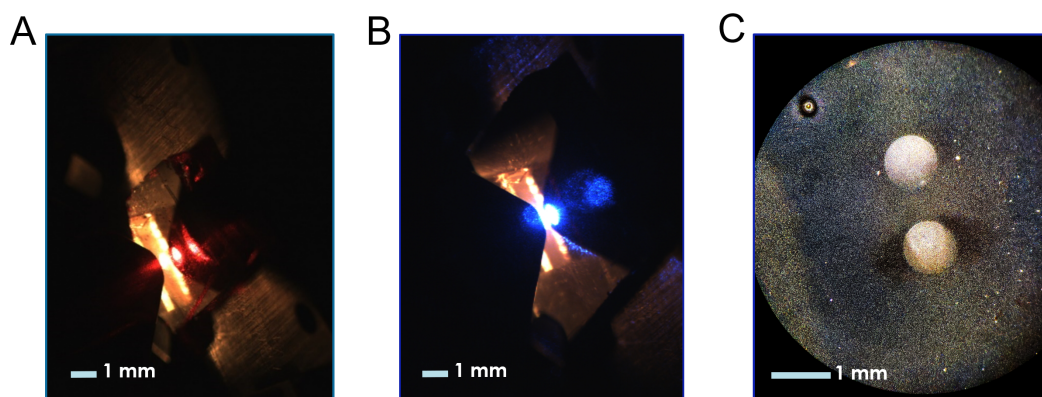


Figure S3. (A) Perovskite sample spot illuminated by red light with a circular shape (B) Perovskite sample illuminated by blue light with an ovalar shape. (C) Perovskite sample after 20 hr.(top) and 48 hr.(bottom) of exposure to blue light and heat. An upper exposure limit of six hours was sufficient to eliminate X-ray effects and isolate the *in situ* laser exposure effects seen in (C) in Cs:FAPbI₃ for study.

Analysis of XPS data was performed using in house code written in Python. The python code used the NumPy⁵, lmfit⁶, pandas^{7,8}, and Matplotlib⁹ libraries to analyze the data and create graphs. XPS data was fit using the Levenberg–Marquardt method of non-linear least squares regression with a tightly constrained asymmetric Voigt model. Note the presence of some PbI₂ spectral intensity in both fresh Cs:FAPbI₃ samples, which could not be eliminated by increasing the asymmetry of the dominant peak shape. The I:Pb ratio was calibrated based on measurements taken on several pure PbI₂ films made for this

purpose. That result provided improved accuracy for the HiPP3 XPS transmission function which was applied to correct the N 1s intensity. The corrected intensities were used to calculate the ratios in Table S1. Note that the I/N levels were typically lower than expected and may be related to large gradients that have been observed in other FAPI thin films.¹⁰

Table S1. Elemental ratios for MHP samples before degradation measured at the same spots for each degraded sample and averaged with different pieces of the same samples tested in this study.

Sample	Fresh	
	I/Pb	N/Pb
h-I	3.8 ± 0.3	2.3 ± 0.2
ns-I	2.8 ± 0.2	2.0 ± 0.2

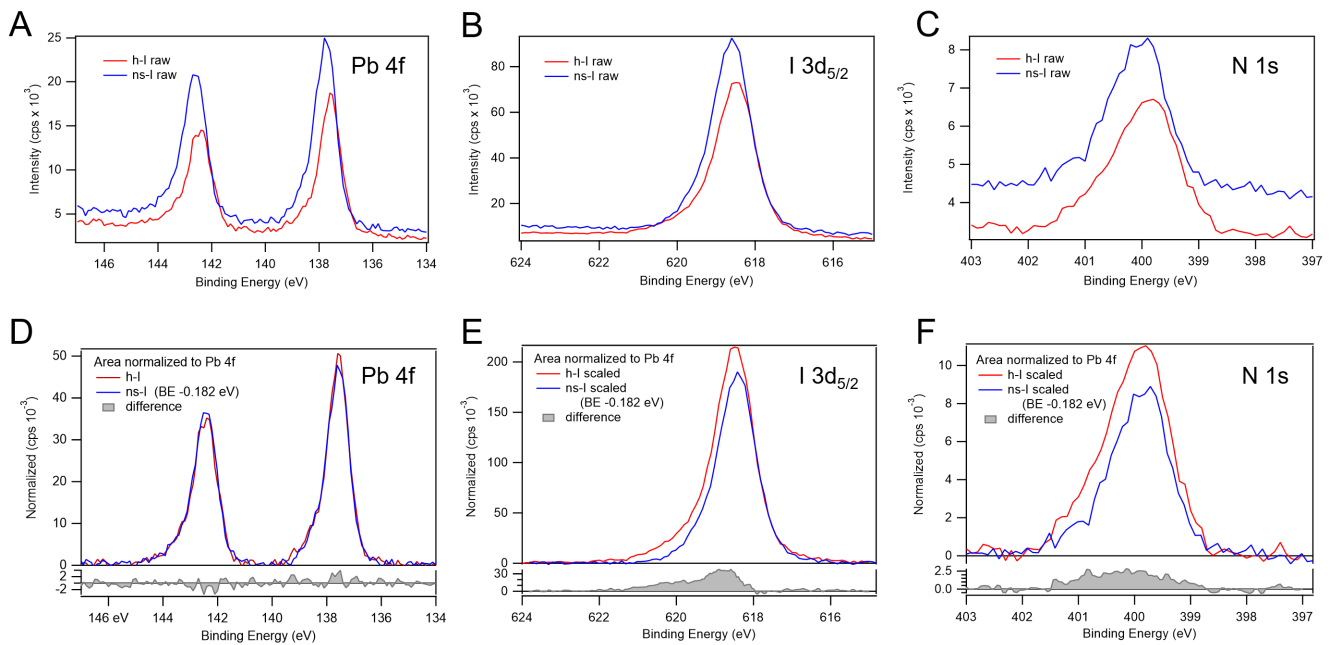


Figure S4. Raw XPS data for h-I and ns-I samples with core levels labeled in A, B and C. D) Core level XPS Pb 4f spectra with areas normalized to unity and ns-I peak shift indicated. E) I $3d_{5/2}$ and F) N 1s spectra shifted and normalized according to Pb 4f BE shift and normalization factors.

Spectral differences are shown in Figure S4. To produce these difference plots, the spectra were corrected for the systematic peak shifts that result from factors such as surface photovoltage, back contact quality, impurities and defects. The Pb 4f was used to both normalize the areas and shift the raw spectra. Two additional spectral components were found in the I $3d_{5/2}$ difference plot in Figure S4E located at slightly higher BE than the main centroid, and another ca. 2 eV above the main peak. These off-center spectral features support the existence iodine and triiodide in the h-I perovskite. In the N 1s difference spectra a broad increase in signal is observed supporting an excess of FA^+ in the h-I films.

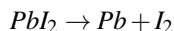
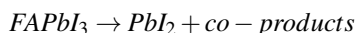
5 Avrami-Erofe'ev Analysis

The general form of the Avrami-Erofe'ev equation is:

$$[A] = [B]_0 - \Delta[B](1 - e^{-(kt)^n}) \quad (3)$$

Where A is the concentration of the initial material, B is total change of material concentration during the experiment, k is the rate constant, t is time, n is the Avrami parameter.

The Avrami-Erofe'ev equations were applied to the observable lead-containing phases utilizing reactions for perovskite to PbI_2 and PbI_2 to $Pb(0)$. The reactions are:



The resulting Avrami-Erofe'ev equations are:

$$[FAPbI_3] = [FAPbI_3]_{t=inf} + \Delta[FAPbI_3]e^{-(k_1t)^n}$$

$$[PbI_2] = -\frac{k_1^n}{k_2^n - k_1^n} \Delta[FAPbI_3]e^{-(k_1t)^n} + ([PbI_2]_{t=0} - \frac{k_1^n}{k_2^n - k_1^n} \Delta[FAPbI_3])e^{-(k_2t)^n}$$

$$[Pb] = -\frac{k_2^n}{k_2^n - k_1^n} \Delta[FAPbI_3]e^{-(k_1t)^n} - ([PbI_2]_{t=0} - \frac{k_1^n}{k_2^n - k_1^n} \Delta[FAPbI_3])e^{-(k_2t)^n} + [Pb]_{t=0} + [PbI_2]_{t=0} + \Delta[FAPbI_3]$$

Where subscripts $t=0$ and $t=inf$ represent initial and final concentrations, and $\Delta[FAPbI_3]$ is the amount of perovskite loss.

Note that one can reliably determine k_2 and n simultaneously if an s-kink is observed or if the reaction is observed near to completion. n has the largest relative error of any of the parameters in the fit routine, and it was ± 0.05 for h-i. This is a measure of the uniqueness of the fit. Higher n values provided larger chi square values. Fit results are shown below.

Table S2. Avrami-Erofe'ev coupled two step reaction fit results.

	$k_1 (\chi/min)$	$k_2 (\chi/min)$	n	$[FAPbI_3]_{t=inf}(\chi)$	$\Delta[FAPbI_3](\chi)$	$[PbI_2]_{t=0}(\chi)$	$[Pb]_{t=0}(\chi)$
h-1 (blue)	0.0139 ± 0.0002	0.00916 ± 0.00010	2.75 ± 0.14	0.226 ± 0.003	0.648 ± 0.011	0.100 ± 0.008	-0.00389 ± 0.00280
ns-1 (blue)	0.000288 ± 0.000008	0.00144 ± 0.00001	1	0	0.794 ± 0.004	0.198 ± 0.001	0.00396 ± 0.00123
Dark	0.0000551 ± 0.0000173	0	1	0	0.841 ± 0.010	0.153 ± 0.005	0.00397 ± 0.00025
Red	0.00532 ± 0.00062	0.000436 ± 0.000031	1	0.788 ± 0.004	0.200 ± 0.014	-0.00206 ± 0.00328	0.0122 ± 0.0004

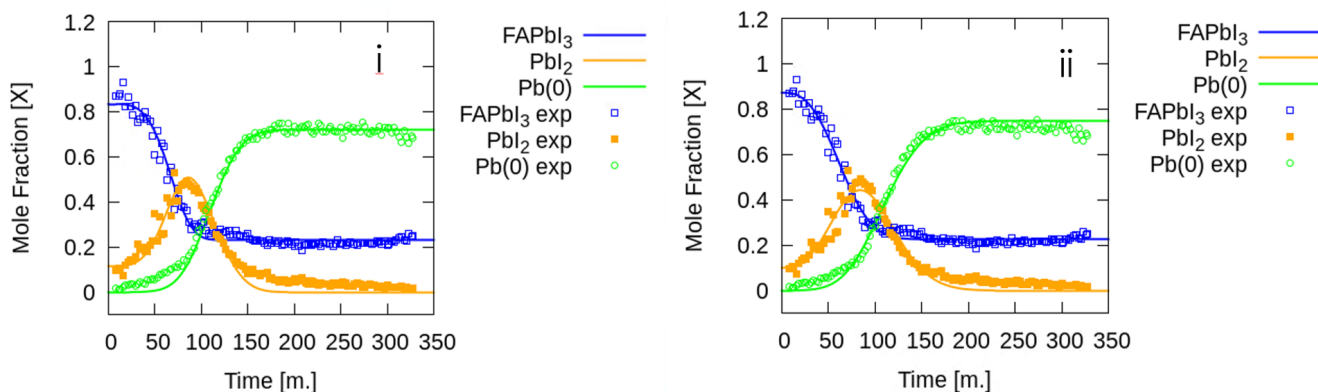


Figure S5. Avrami-Erofe'ev coupled two step reaction fits with n allowed to fit to 2.78 (i) compared to n held fixed at 4.0 (ii).

6 Cs:FAPbI₃ Exposure to Red vs. Blue Light

The evolution of Pb(0) peak intensity for the h-I sample under dark, red, and blue light exposure at 69 C is shown in Figure S6. For blue light, the Pb(0) feature growth shows a sigmoidal curve shape with the fastest growth around 100 minutes and leveling off at a mole fraction of nearly 0.8 by 200 minutes. Under red exposure, Pb(0) mole fraction does not exceed 0.05 over 300 minutes. The red light exposure slightly accelerates Pb(0) growth relative to dark.

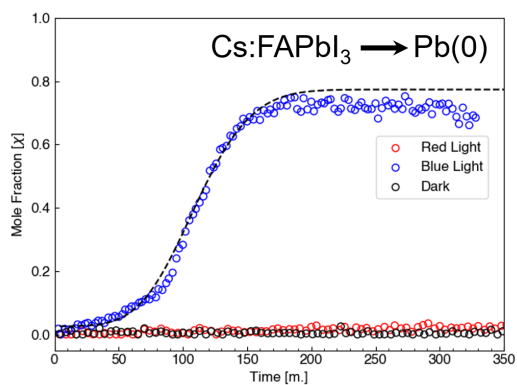


Figure S6. Pb 4f fit area results showing Pb(0) molar fraction increasing over time during accelerated degradation tests of Cs:FAPbI₃ comparing dark, red and blue light exposure conditions for perovskite films. Surface temperature was 69°C.

7 PbI₂ Exposure to Red vs. Blue Light

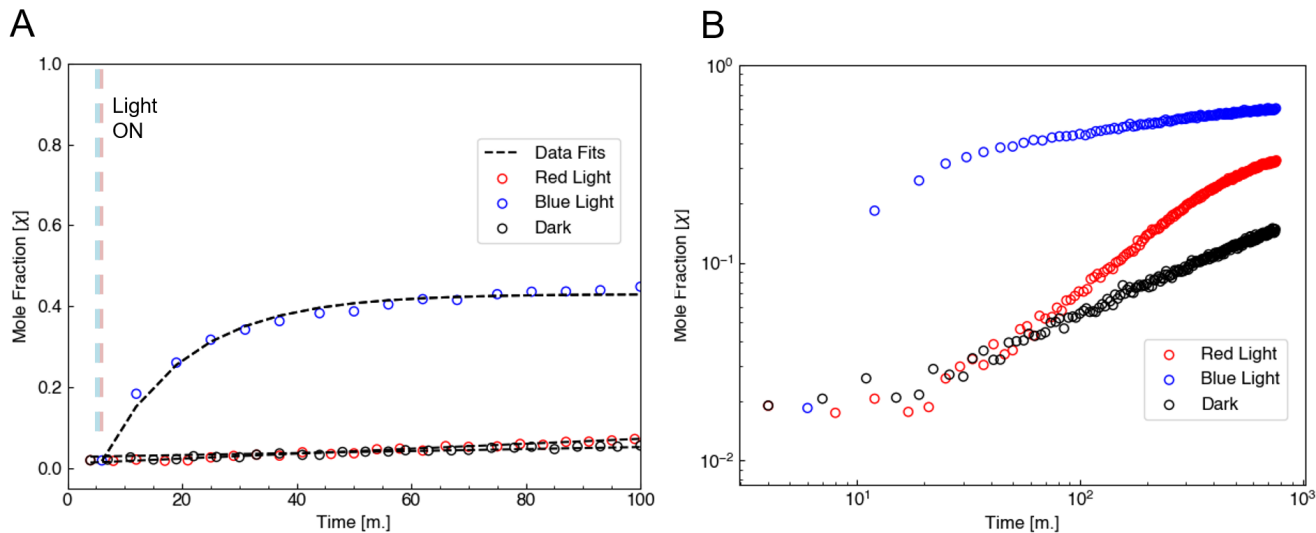


Figure S7. Time resolved *in situ* XPS results for the degradation neat PbI₂ films showing fitted Pb 4f Pb(0) peak area results. A) Pb(0) intensity for first 100 minutes of exposure of perovskite to red, blue and dark conditions. B) Log-log plot of long exposure times for red, blue and dark conditions. Surface temperature was 69°C.

A study of neat PbI₂ films was done to examine the lead halide's response in identical experimental conditions as the perovskite. Results of dark, red and blue light exposure of PbI₂ samples are shown in Figure S7. Surface temperature was 69°C for all measurements. Figure S7A shows early changes to Pb(0) intensity versus time. The decomposition of PbI₂ evolves slowly in dark conditions with mild heat and typical X-ray exposure. Addition of red light increases Pb(0) signal slightly in this time frame. Blue light exposure results in immediate and rapid increase of Pb(0). Figure S7B shows much longer exposure of PbI₂ to blue, red and dark conditions. Note that the blue light exposure of PbI₂ results in rapid Pb(0) signal increase relative to dark and red conditions. However, it is also clear that red light increases Pb(0) intensity over this longer time frame and deviates from the dark result. Red light exposure also has a different curve shape relative to the blue light exposure, presumably due to an increasing density of photoactive X-ray induced point defects. Light initiated growth of Pb(0) for 473 nm and 671 nm illumination at equal power densities (1000 mW/cm²) were fit with reaction-order kinetic models¹¹. Blue light reaction dependence following the equation $A(1 - \exp(-kt))$ whereas the red light and dark conditions appear to be linear following the equation $kt + b$. The first-order reaction model depends on a factor A which scales the fit to the point where the data levels off, and the reaction rate k which gives insight to the difference between blue and red light induced degradation. During the photolysis of PbI₂ blue light creates more electron-hole pairs which participate in greater surface recombination and reactions than red light due to having higher photon absorption efficiency in the thin film.¹² The blue light exposure results in a reaction rate of $0.066 \chi/\text{min} \pm 0.004$, which is significantly higher than the restricted growth rate found for Cs:FAPbI₃. The dark condition is shown with black circle markers. Roughly half of the Red laser induced Pb(0) signal can be attributed to the X-ray exposed sample being heated in vacuum conditions. The red light exposure yields a reaction rate of $.0006 \chi/\text{min} \pm .000003$, also higher than the Cs:FAPbI₃ result. The dark exposure yields $.0002 \chi/\text{min} \pm .000005$. A close look at the red data also suggests a delay in the increase of Pb(0) intensity which may be related to the slow population of X-ray induced defects. These data confirm rapid decomposition of PbI₂ due to blue light in the current experimental conditions.

Acknowledgements

This work is funded by the U.S. Department of Energy Solar Energy Technologies Office, under Award Number DE-EE0008540.

References

1. Irwin, M. D., Dhas, V. V. & Mielczarek, K. Doped nickel oxide interfacial layer. US10189998B2 (2019).
2. Irwin, M. D., Chute, J. A. & Dhas, V. V. Method of formulating perovskite solar cell materials. US9305715B2 (2016).
3. Irwin, M. D., Chute, J. A. & Dhas, V. V. Perovskite material layer processing. US9425396B2 (2016).
4. Irwin, M. D., Chute, J. A., Dhas, V. V. & Mielczarek, K. Mixed cation perovskite material devices. US10316196B2 (2019).
5. Oliphant, T. NumPy: A guide to NumPy. USA: Trelgol Publishing (2006–). [Online; accessed 05/2020].
6. Newville, M., Stensitzki, T., Allen, D. B. & Ingargiola, A. LMFIT: Non-Linear Least-Square Minimization and Curve-Fitting for Python, DOI: 10.5281/zenodo.11813 (2014).
7. Wes McKinney. Data Structures for Statistical Computing in Python. In Stéfan van der Walt & Jarrod Millman (eds.) *Proceedings of the 9th Python in Science Conference*, 56 – 61, DOI: 10.25080/Majora-92bf1922-00a (2010).
8. pandas development team, T. pandas-dev/pandas: Pandas, DOI: 10.5281/zenodo.3509134 (2020).
9. Hunter, J. D. Matplotlib: A 2d graphics environment. *Comput. Sci. Eng.* **9**, 90–95 (2007).
10. Harvey, S. P., Messinger, J., Zhu, K., Luther, J. M. & Berry, J. J. Investigating the Effects of Chemical Gradients on Performance and Reliability within Perovskite Solar Cells with TOF-SIMS. *Adv. Energy Mater.* **10**, 1903674, DOI: 10.1002/aenm.201903674 (2020). [_eprint: https://onlinelibrary.wiley.com/doi/pdf/10.1002/aenm.201903674](https://onlinelibrary.wiley.com/doi/pdf/10.1002/aenm.201903674).
11. Khawam, A. & Flanagan, D. R. Solid-State Kinetic Models: Basics and Mathematical Fundamentals. *The J. Phys. Chem. B* **110**, 17315–17328, DOI: 10.1021/jp062746a (2006).
12. Albrecht, M. *The Photolysis of Lead Iodide*. Ph.D. thesis, University of London, Imperial College, South Kensington, London SW7 2BU, United Kingdom (1975).